

Surface Tongue-and-groove Contours on Lens MIP Facilitate Cell-to-cell Adherence

Dimitrios Fotiadis¹, Lorenz Hasler¹, Daniel J. Müller¹
Henning Stahlberg¹, Jörg Kistler² and Andreas Engel^{1*}

¹*M. E. Müller-Institute for Microscopy at the Biozentrum University of Basel, CH-4056, Basel, Switzerland*

²*School of Biological Sciences University of Auckland Auckland, New Zealand*

The lens major intrinsic protein (MIP, AQP0) is known to function as a water and solute channel. However, MIP has also been reported to occur in close membrane contacts between lens fiber cells, indicating that it has adhesive properties in addition to its channel function. Using atomic force and cryo-electron microscopy we document that crystalline sheets reconstituted from purified ovine lens MIP mostly consisted of two layers. MIP lattices in the apposing membranes were in precise register, and determination of the membrane sidedness demonstrated that MIP molecules bound to each other *via* their extracellular surfaces. The surface structure of the latter was resolved to 0.61 nm and revealed two protruding domains providing a tight “tongue-and-groove” fit between apposing MIP molecules. Cryo-electron crystallography produced a projection map at 0.69 nm resolution with a mirror symmetry axis at 45° to the lattice which was consistent with the double-layered nature of the reconstituted sheets. These data strongly suggest an adhesive function of MIP, and strengthen the view that MIP serves dual roles in the lens.

© 2000 Academic Press

Keywords: atomic force microscopy; aquaporins; major intrinsic protein; sidedness; two-dimensional crystals

*Corresponding author

Introduction

The major intrinsic protein (MIP) has a lively past: initially isolated and cloned from the bovine lens (Broekhuysse *et al.*, 1976; Gorin *et al.*, 1984), it is now recognized as the founding member of the MIP family of water and solute channels (Park & Saier, 1996; Lee *et al.*, 1997). MIP, also referred to as AQP0, increases membrane permeability for water and glycerol (Kushmerick *et al.*, 1995; Mulders *et al.*, 1995; Chandy *et al.*, 1997; Varadaraj *et al.*, 1999), and is as such a component of the micro-circulation system which maintains nutrient and electrolyte homeostasis in the lens (Mathias *et al.*, 1997). This crucial physiological role of MIP is further supported with evidence that mutations in this polypeptide cause cataract (Shiels & Bassnett, 1996).

Though the characterization of MIP specifically as a water and solute channel is relatively recent, less specific channel activities of this integral membrane protein were reported earlier. MIP channels were first characterized in reconstituted liposomes (Gooden *et al.*, 1985; Scaglione & Rintoul, 1989), and later in planar lipid bilayers where it was possible to determine single channel properties (Ehring *et al.*, 1990; Shen *et al.*, 1991; Ehring *et al.*, 1992; Modesto *et al.*, 1996). From the latter studies it was concluded that MIP formed voltage-sensitive non-selective ion channels, a property that was not observed in MIP-expressing oocytes or lens cells. While this discrepancy remains unexplained, it nevertheless re-inforces the characterization of MIP as a membrane channel.

Much of the literature on MIP, however, concerns another function of MIP, as a cell-cell adhesion protein. MIP is enriched in the 11–13 nm “thin” junctional domains connecting lens fiber cells (Bok *et al.*, 1982; Sas *et al.*, 1985). While initially mistaken as communicating junctions, they are clearly distinct from the 16–17 nm “thick” gap junctions composed of the channel-forming connexins (Kistler *et al.*, 1985; Gruijters *et al.*, 1987; Zampighi *et al.*, 1992). MIP containing junctions are

D. F. and L. H. contributed equally to this work.

Abbreviations used: AFM, atomic force microscopy; AQP, aquaporin; FRC, Fourier ring correlation function; MIP, major intrinsic protein; PHR, phase residual; SSNR, spectral signal-to-noise ratio.

E-mail address of the corresponding author: Andreas.Engel@unibas.ch

present in two forms: as straight junctions which contain MIP in both apposing membranes, and as “wavy” junctions where MIP is restricted to the convex membrane (Zampighi *et al.*, 1989). MIP containing junctions are further characterized by the presence of square arrays (Zampighi *et al.*, 1982; Costello *et al.*, 1989).

The junction-forming, adhesive properties of MIP can also be demonstrated *in vitro* by reconstituting it into liposomes which aggregate only when the protein is present (Dunia *et al.*, 1987). This strongly supports a role of MIP in cell-cell adhesion consistent with the extraordinarily narrow extracellular spaces that are so characteristic for the crystalline cellular architecture of lens tissue.

MIP, like other aquaporins (AQPs), is predicted to assume a conformation which has six transmembrane segments, and the amino and carboxy termini located on the cytoplasmic side of the lens fiber cell plasma membrane (Keeling *et al.*, 1983; Gorin *et al.*, 1984). The structure of MIP has recently been resolved in projection at 0.90 nm, and shows significant similarity with AQP1 (Hasler *et al.*, 1998). This projection map was achieved by cryo-electron crystallography of freeze-dried crystalline sheets reconstituted from purified ovine lens MIP and exogenous lipids. We now report on a further analysis of these crystalline MIP sheets by atomic force microscopy (AFM) and cryo-electron crystallography of vitrified samples. We document distinct peptide domain structures at the cytoplasmic and extracellular surfaces, and identify the cytoplasmic

surface in two ways, one by visualizing the loss of peptide mass caused by digesting the carboxyl tail of MIP with carboxypeptidase Y, and two by labeling the sheets with antibodies against the cytoplasmic loop B. In addition, we demonstrate that MIP sheets consist of two crystalline membrane layers with their lattices in precise register and facing each other with their extracellular surfaces. This observation renders further support that MIP has adhesive properties, and strengthens the view that this protein has dual functions.

Results

Visualization of peptide domains of MIP protruding from the membrane

High-resolution AFM imaging was employed to visualize the peptide domains of MIP that protrude from the membrane. Crystalline sheets were adsorbed to freshly cleaved mica and imaged in aqueous solution. Besides the atomically flat mica—three different surfaces were typically observed: the majority of the sheet surface appeared “smooth” and crystalline (Figure 1(a), 1), while smaller areas with a “rough” surface texture were located at the periphery of the sheets and appeared a step down from the “smooth” surface (Figure 1(a), 2). The texture of the “rough” surface ranged from unordered to crystalline, often with continuous transitions. The sheets were surrounded by a third type of surface that had no discernible structural features and probably

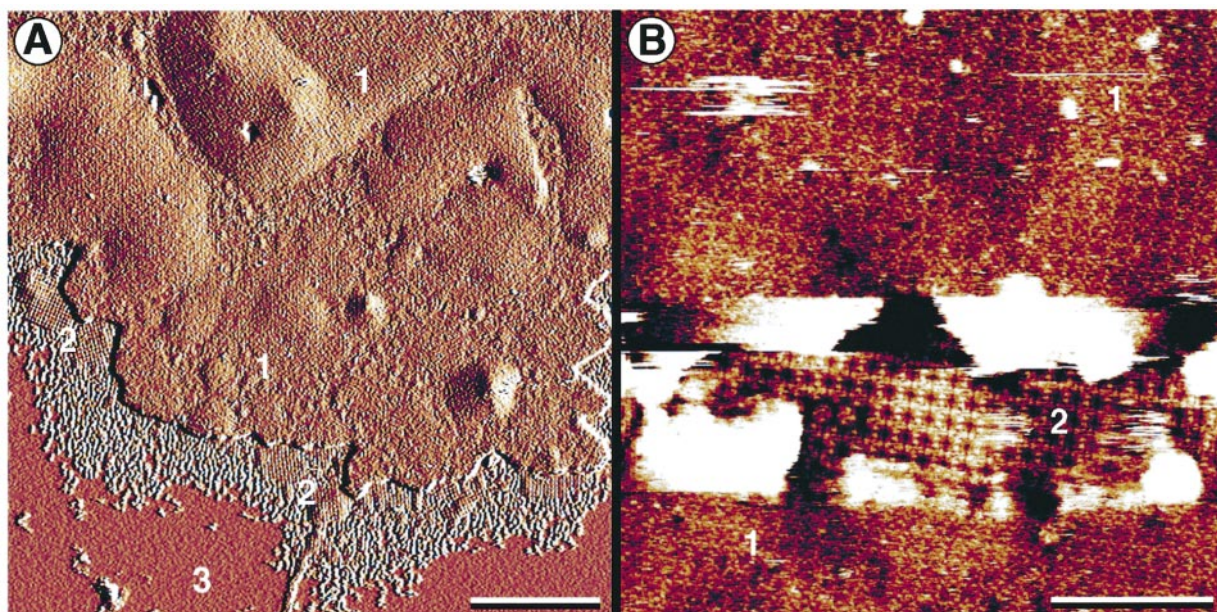


Figure 1. AFM of a reconstituted double-layered MIP sheet on mica. (a) The low-magnification deflection image shows three different regions. (1) A “smooth” crystalline, (2) a “rough” crystalline and (3) a structureless surface. (b) Topographies of both MIP surfaces are visible following the partial removal of the upper layer with the AFM tip. Imaged in buffer A. Scan frequency 5.1 Hz in (a) and (b). The scale bar represents 250 nm in (a) and 50 nm in (b). The vertical brightness range of the height topograph in (b) is 1.8 nm.

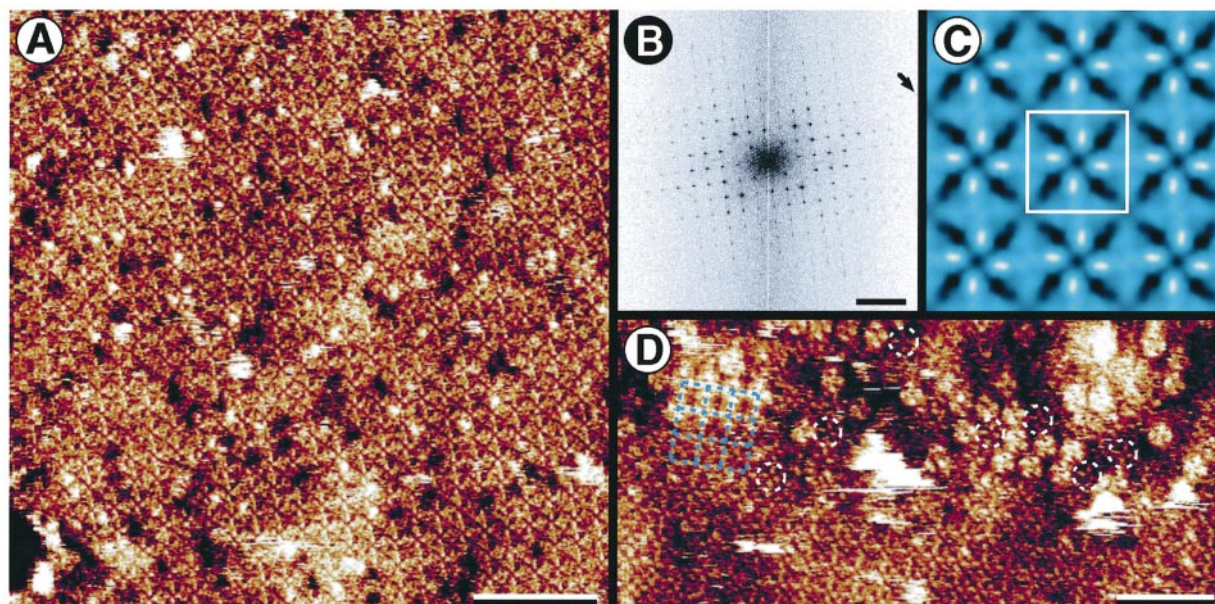


Figure 2. The “smooth” surface of MIP. (a) Raw image of the “smooth” surface of MIP. (b) The powerspectrum of the raw image exhibits diffraction spots to order (10,3) corresponding to a lateral resolution of 0.61 nm. (c) The symmetrized correlation average (RMSD of 18% from the 4-fold symmetry) of 542 unit cells reveals four major globular protrusions of $0.8(\pm 0.1)$ nm ($N = 80$) height surrounding a distinct central cavity, and four diagonal elongated depressions per tetramer. (d) The unit cell marked in the average (c) was defined using the structure information available from single unordered tetramers in densely packed non-crystalline regions (broken white circles) and from packing defects of “rough”-sided tetramers in the crystal lattice. Imaged in buffer A. Scan frequencies: (a) 6.1 Hz and (d) 5.5 Hz. The scale bar represents 35 nm in (a), 2 nm^{-1} in (b) and 25 nm in (d). The frame size of the average (c) is that of three unit cells, 19.2 nm. Vertical brightness ranges (a) 1.0 nm, (c) 0.8 nm and (d) 1.5 nm.

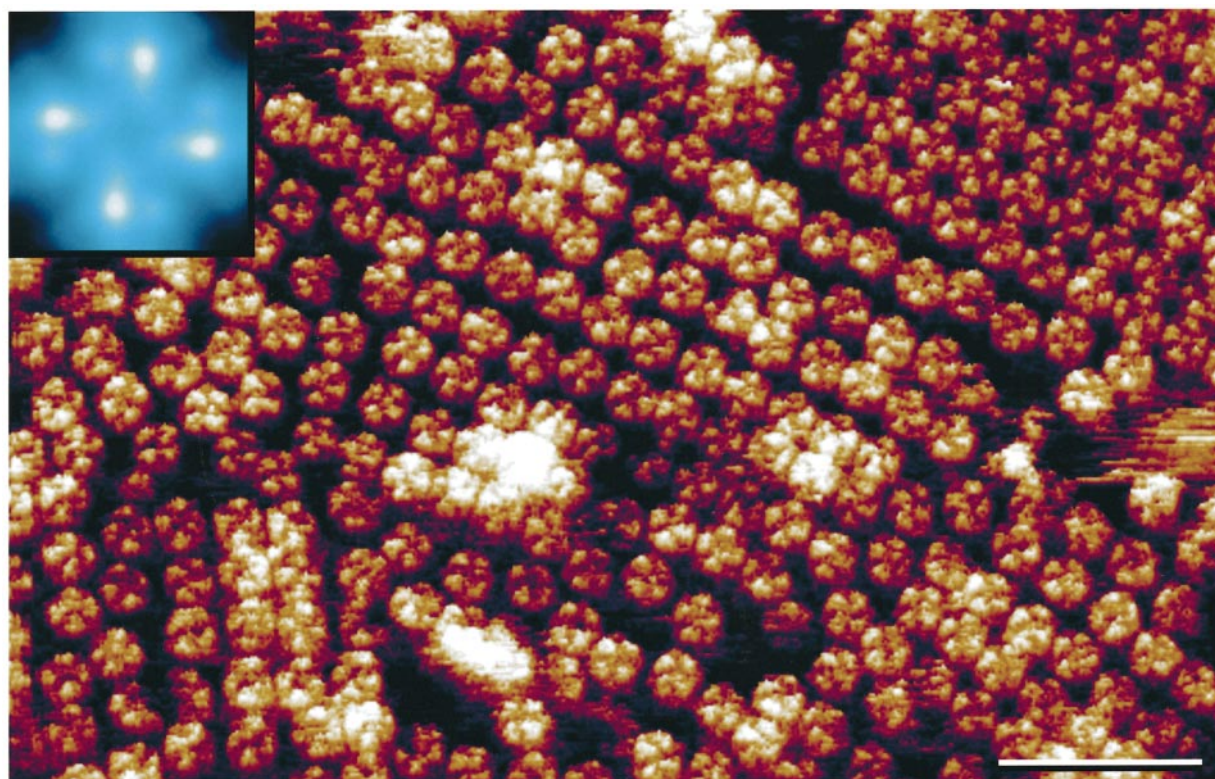


Figure 3. The “rough” surface of MIP. Beside crystalline lattices (top right), densely packed non-crystalline regions exhibiting individual MIP tetramers were visualized by AFM. Inset: the correlation average of 445 unit cells exhibited a RMSD of 7% from the 4-fold symmetry. Imaged in buffer B. Scan frequency 4.7 Hz. The scale bar represents 25 nm. The frame size of the inset is that of one unit cell, 6.4 nm. The vertical brightness range of the raw image is 1.6 nm and for the inset 1.4 nm. The raw image is displayed as relief tilted by 2° .

represented lipid bilayer regions without protein (Figure 1(a), 3).

In order to image larger areas of the "rough" surface, the top layer was scraped away by scanning a selected area with a higher force applied to the tip (Hoh *et al.*, 1991; Schabert *et al.*, 1995). A typical experiment is shown in Figure 1(b). An area just below the middle of the image was first scanned with a force of 500-750 pN to remove the top layer, and then imaged at minimal force of 50-150 pN. The lower layer had a rough-crystalline texture which was identical with that seen in the peripheral regions of the sheets (Figure 1(a), 2). Examining Figure 1(b) at glancing angles reveals that the lattices of the smooth-crystalline top layer and the rough-crystalline lower layer are stacked in register.

From a number of buffers tested, the best images of the smooth surface were obtained using 10 mM Tris-HCl (pH 8.8), 150 mM KCl, 50 mM MgCl₂ (buffer A; Figure 2). Diffraction spots extended to order (10,3) of the square lattice representing a lateral resolution of 0.61 nm (Figure 2(b)). The correlation average of the smooth side of the MIP tetramer revealed a major globular protrusion of $0.8(\pm 0.1)$ nm ($N=80$) height per monomer (Figure 2(c)). "Crystal defects" resulting from the packing of tetramers with the rough side facing up (lattice; Figure 2(d)) and the morphology of single smooth-sided tetramers (broken white circles; Figure 2(d)) in disordered patches allowed the unit cell in the correlation-averaged image (Figure 2(c)) to be defined. The resolution of the latter was 0.7 nm according to the Fourier ring correlation function (FRC; Saxton & Baumeister, 1982), and 0.8 nm according to the phase residual (PHR; Frank *et al.*, 1981).

Large selected areas of the rough surface could be imaged following the removal of the top layer with the AFM tip. Scraping away the upper layer was easier to achieve using a different buffer with reduced pH and salt (buffer B: 20 mM Na-acetate-HCl (pH 5.0), 50 mM NaCl). Contamination of the tip during scanning was diminished drastically using buffer B. The lower layer remained firmly attached to the mica support and could be imaged at high resolution equally in buffers A or B. The rough surface exhibited crystalline areas, regions of densely packed tetramers, and regions with loosely packed tetramers with a distinct "windmill" appearance (Figure 3). Scraping away the top layer often disturbed the crystalline order by introducing small cracks into the lower layer, and this limited the application of correlation averaging. Instead, we focused on areas with densely packed tetramers for structure determination using single particle analysis (Frank *et al.*, 1978; Schabert & Engel, 1994). The resolution was 0.6 nm according to both the FRC (Saxton & Baumeister, 1982) and the PHR (Frank *et al.*, 1981), and 0.8 nm according to the spectral signal-to-noise ratio (SSNR; Unser *et al.*, 1987). The average of the rough side of the MIP tetramer showed two protrusions per monomer, a

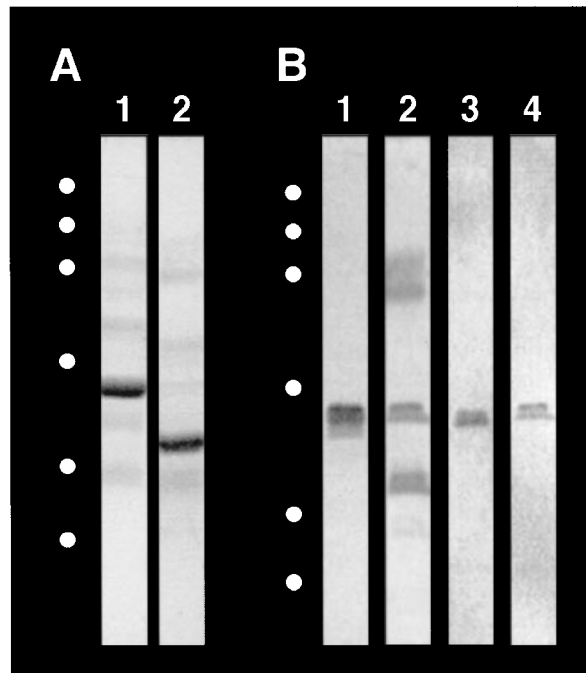


Figure 4. *In vitro* carboxypeptidase Y digestion of urea/alkali-stripped membranes and reconstituted 2D MIP crystals. (a) Coomassie blue-stained SDS/15% (w/v) polyacrylamide gel of urea/alkali-stripped membranes. Lane 1, Urea/alkali-stripped membranes, incubated overnight at room temperature without carboxypeptidase Y, demonstrating the presence of a single major band below 30 kDa. Lane 2, urea/alkali-stripped membranes incubated overnight with 250 units of carboxypeptidase Y at room temperature. After digestion membranes were washed to remove the remaining carboxypeptidase Y. (b) Silver-stained SDS/15% (w/v) polyacrylamide gel of reconstituted 2D crystals of MIP. Lane 1, MIP 2D crystals incubated overnight at room temperature without carboxypeptidase Y. Lane 2, MIP 2D crystals incubated overnight with 250 units of carboxypeptidase Y at room temperature. Partial digestion is indicated by the major bands below 30 kDa and at approximately 23 kDa. The broad protein band at 43 kDa represents the remaining carboxypeptidase Y. Lane 3, immunoblot analysis against the carboxyl tail of the undigested 2D crystal identifies the major band below 30 kDa as MIP. Lane 4, immunoblot analysis against the carboxyl tail of the digested MIP 2D crystals. Molecular mass standards marked by filled circles are (from top to bottom) 94, 66, 43, 31, 21, and 14 kDa.

small globular and a larger elongated domain (Figure 3, inset). The heights of these domains varied slightly depending on whether measurements were taken from MIP tetramers in crystalline or densely packed areas, and on the buffer used for imaging (Table 1). Average heights of the large and small domains were $1.4(\pm 0.2)$ nm ($N=120$) and $1.1(\pm 0.2)$ nm ($N=120$), respectively. Hence, the MIP monomer has two peptide domains protruding from the rough surface which are both significantly higher than the single domain visible on the smooth surface, meaning that the distribution

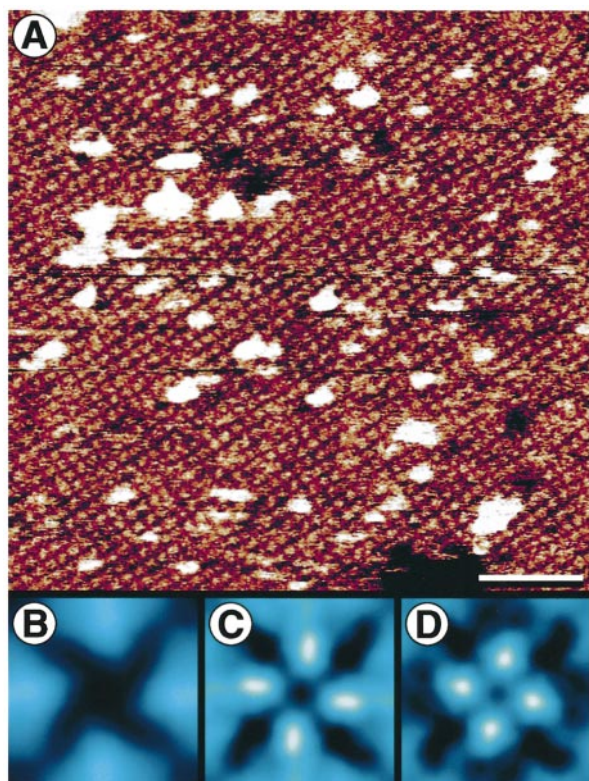


Figure 5. The “smooth” surface of MIP following digestion by carboxypeptidase Y on mica. (a) The raw image reveals significantly altered surface features compared to the undigested surface shown in Figure 2(a). A pronounced decrease in height from $0.8(\pm 0.1)$ nm ($N = 80$) to $0.6(\pm 0.1)$ nm ($N = 80$) and a wider cavity are characteristic for this new surface structure. (b) In the 4-fold symmetrized correlation average (RMSD of 15% from the 4-fold symmetry) of 508 unit cells, the absence of the prominent, initially existing protrusion (c) is clearly visible. (d) Difference map between the (c) undigested and (b) digested, cytoplasmic surface. This result identifies the “smooth” surface as the cytoplasmic side, and further localizes the C terminus of MIP. Imaged in buffer A. Scan frequency 6.1 Hz. The scale bar represents 35 nm in (a). (b)-(d) The frame sizes are that of one unit cell, 6.4 nm. Vertical brightness ranges: (a) 1.0 nm; and (b)-(d) 0.8 nm.

of peptide mass with respect to the membrane plane is strongly asymmetric.

Lipid bilayers with or without MIP also showed different heights depending on the buffer used for imaging. When imaged in buffer A, the height of the double-layered MIP crystal was $13.1(\pm 0.3)$ nm ($N = 80$) and the lipid alone exhibited a height of $4.5(\pm 0.2)$ nm ($N = 120$). In buffer B the double-layered sheets had a height of $10.0(\pm 0.4)$ nm ($N = 120$), while a single lipid bilayer had a height of $2.9(\pm 0.2)$ nm ($N = 126$). These height differences measured in the different buffers are consistent with a change of the electrostatic tip-sample interaction (Müller & Engel, 1997).

Table 1. Heights of the protrusions on the “rough” surface measured in two imaging buffers

Imaging buffer	Large elongated domain (nm)	Small globular domain (nm)
A	$1.6(\pm 0.2)^a$ ($N = 80$)	$1.3(\pm 0.2)^a$ ($N = 80$)
	$1.4(\pm 0.2)^b$ ($N = 120$)	$1.1(\pm 0.2)^b$ ($N = 120$)
B	$1.4(\pm 0.1)^a$ ($N = 80$)	$1.1(\pm 0.1)^a$ ($N = 80$)
	$1.2(\pm 0.1)^b$ ($N = 80$)	$1.0(\pm 0.1)^b$ ($N = 80$)

A 10 mM Tris-HCl (pH 8.8), 150 mM KCl, 50 mM MgCl₂; B 20 mM Na-acetate-HCl (pH 5), 50 mM NaCl. Heights were measured on densely packed regions and on crystalline regions, respectively.

^a Densely packed region.

^b Crystalline region.

Identification of the “smooth” surface as cytoplasmic

The topology for MIP predicted from the amino acid sequence places the approximately 5 kDa carboxyl tail segment on the cytoplasmic side of the lens fiber cell plasma membrane (Gorin *et al.*, 1984). The same conclusion was reached by probing MIP in isolated membranes with site-specific proteolysis and antibodies (Keeling *et al.*, 1983).

Removal of the carboxyl tail segment of lens fiber membrane proteins was first investigated on alkali/urea-stripped membranes. To this end, membranes were incubated with carboxypeptidase Y overnight at room temperature (see Materials and Methods) and analyzed by SDS-PAGE. As a negative control, membranes were incubated without carboxypeptidase Y, yielding the major band below 30 kDa in Figure 4(a) (lane 1) which represents native MIP. After overnight digestion of stripped membranes with carboxypeptidase Y a clear shift of the major band to approximately 23 kDa was observed (Figure 4(a), lane 2). The same experiment was also carried out with reconstituted MIP lattices (Figure 4(b)). The 2D crystals, which were incubated without carboxypeptidase Y, exhibited a major band below 30 kDa on the gels (Figure 4(b), lane 1). Carboxypeptidase Y digestion of the 2D crystals resulted in a band-shift to approximately 23 kDa, whereas the remaining band below the 30 kDa indicated that the digestion was not completed (Figure 4(b), lane 2). The subsequent immunoblot analysis with an antibody against the carboxyl tail of MIP confirmed that the carboxypeptidase Y digestion indeed removed exclusively the carboxyl tail (Figure 4(b), lane 4).

According to the *in vitro* experiments, the elimination of the carboxyl tail segment of MIP with carboxypeptidase Y should result in a detectable loss of peptide mass in one of the topographs of MIP, thereby identifying either the smooth or the rough surface as cytoplasmic. Sheets were digested on mica overnight (see Materials and Methods) and subsequently imaged by AFM in buffer A. Only the structure of the smooth surface was distinctly altered by the carboxypeptidase Y treatment: its crystalline texture appeared coarser (Figure 5(a)),

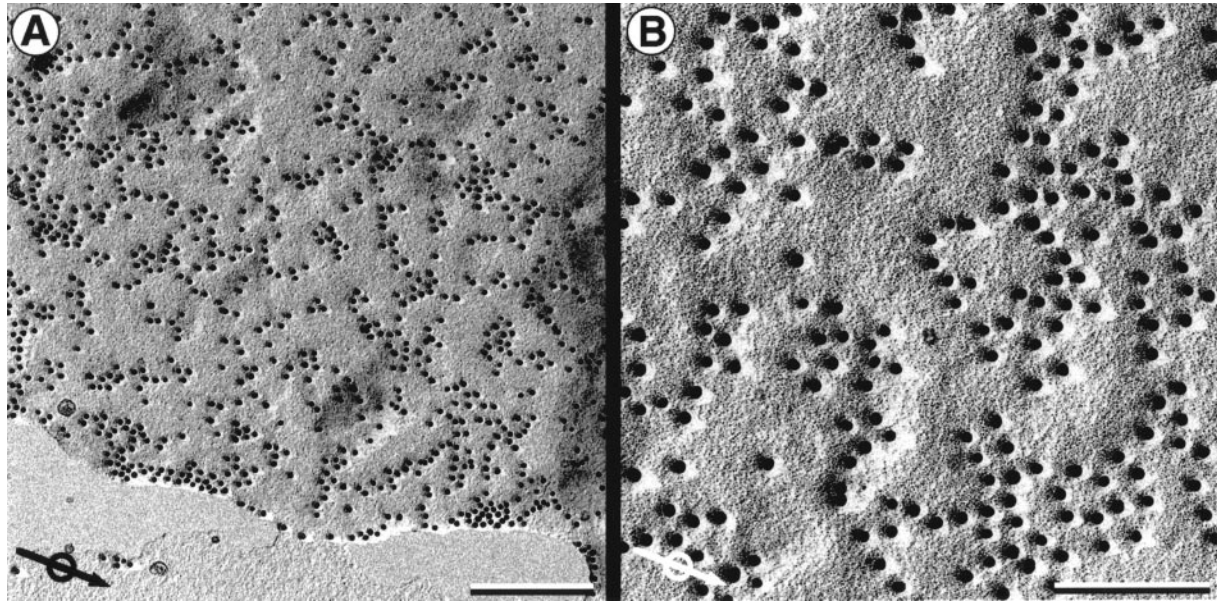


Figure 6. Immunogold labeling of MIP crystalline sheets with subsequent Pt/C metal shadowing. (a) An overview showing the labeling of a sheet with adjacent mica background. Few gold particles were detected in the background, demonstrating the high specificity of the HNPA1 antibody for MIP. (b) Region labeled with gold particles at higher magnification. Note that the particles have a bright, sharp shadow of length similar to those on the mica, indicating that they are bound to the top surface and are not buried between membrane layers. The scale bar represents 400 nm in (a) and 75 nm in (b). The arrows in (a) and (b) indicate the shadowing direction.

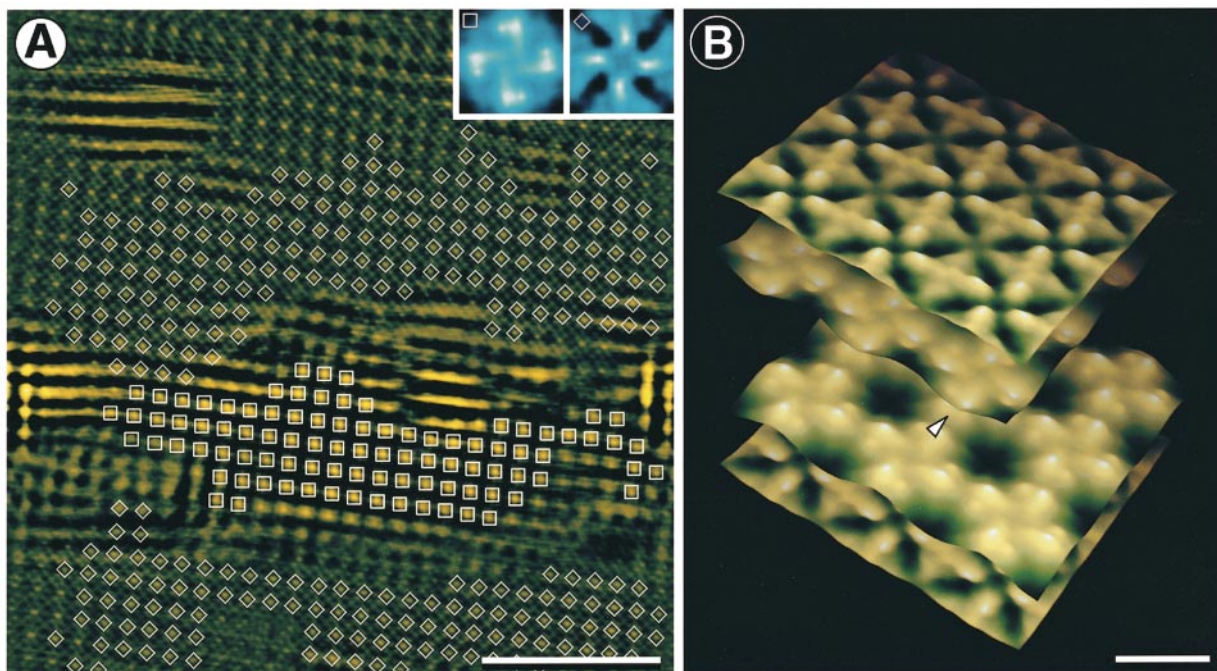


Figure 7. The in-register superposition of two crystalline layers in reconstituted MIP sheets. (a) The cross-correlation function of Figure 1(b) with the sum of the extracellular (inset: square) and cytoplasmic (inset: diamond) surface topographs. The correlation peaks mark the positions of all MIP tetramers and show that they are in precise register. Peaks with a RMSD of less than 10% from the fitted crystal lattice are highlighted by squares (extracellular surface) or diamonds (cytoplasmic surface). (b) Computer reconstruction of a double-layered MIP sheet showing the "tongue-and-groove" interaction of the extracellular surfaces (white arrowhead). The scale bar represents 50 nm in (a) and 5 nm in (b). The frame size of the insets in (a) is that of one unit cell, 6.4 nm. Vertical brightness ranges: 1.4 nm ((b) and inset, square) and 0.8 nm (inset, diamond).

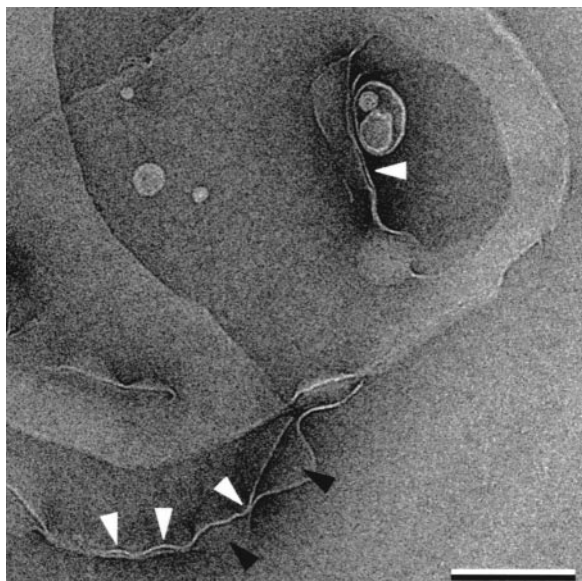


Figure 8. Cryo-negative stain of reconstituted MIP sheets revealing their double membrane nature. Two layers can clearly be recognized at the borders of the sheets (white arrowheads). Apposing membranes are sometimes slightly opened at their edges and expose single layers (black arrowheads). The scale bar represents 200 nm.

and the averaged tetramer structure revealed the partial loss of the prominent four protrusions leaving a large cavity about the 4-fold symmetry axis (Figure 5(b)). Compared to the situation before digestion (Figure 5(c)), the remaining protruding mass was located more peripherally in the tetramer, and had a height of $0.6(\pm 0.1)$ nm ($N = 80$).

The difference map between the undigested and the digested cytoplasmic topographs (Figure 5(d)) reveals that the carboxyl tail is located close to the center of the MIP tetramer. In contrast to this readily detectable structure change in the smooth surface, the rough surface of the membranes did not appear to be affected by the carboxypeptidase Y treatment (data not shown).

The sidedness of the reconstituted sheets was also determined by immunogold labeling. HNPA1, an antibody against the cytoplasmic loop B, was bound to sheets adsorbed to mica and detected with a gold-labeled secondary antibody. A Pt/C replica was produced and examined by electron microscopy (Figure 6). The shadow casts of the gold beads had the same lengths irrespective of their location on sheets or mica, thus indicating that they were bound to the top surface of the sheets and not buried between the two crystalline layers. This result also identified the top surface as cytoplasmic in agreement with the AFM data.

Structural interactions between the extracellular surfaces of MIP

A survey by AFM showed that the majority of reconstituted sheets consisted of two crystalline layers. To demonstrate that the lattices of the two membranes were in precise register, the cross-correlation function of Figure 1(b) with the sum of the averages from both surface structures (Figure 2(c) and the inset in Figure 3) was calculated. Correlation peaks in Figure 7(a) mark the position of all MIP tetramers. Peaks with a RMSD of less than 10% from the fitted crystal lattice are highlighted by squares ($N = 92$) on the extracellular surface and by diamonds ($N = 278$) on the cytoplasmic surface. The large number of such peaks indicated

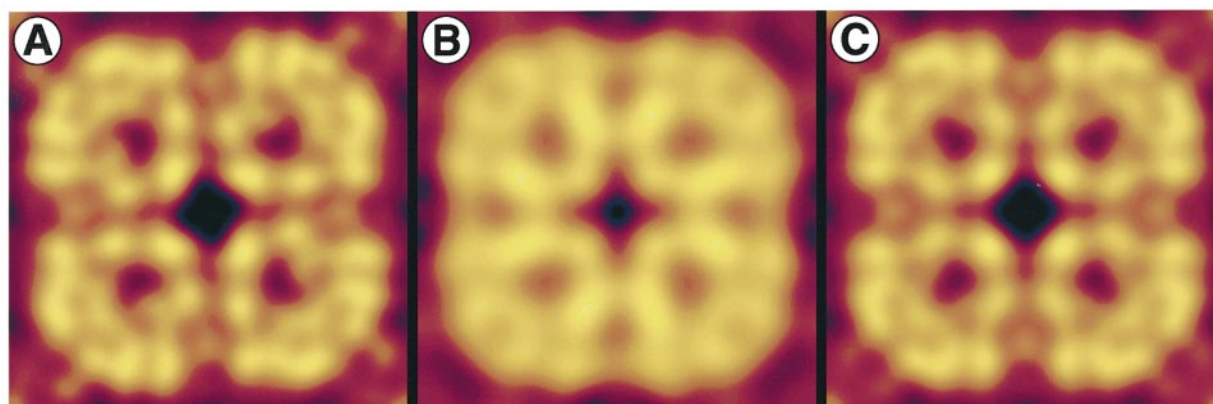


Figure 9. Two distinct projection maps of MIP tetramers determined by cryo-electron crystallography. (a) One type of projection map shows eight density peaks per MIP monomer and exhibits a distinct handedness. A resolution of 0.57 nm was achieved. The seven electron micrographs used to calculate the map were most probably recorded from single-layered sheets. (b) The other type of projection map exhibits eight densities in the monomer which are symmetrically arranged with respect to a mirror plane at 45° to the lattice. The image has 0.69 nm resolution and was calculated from five micrographs most likely depicting the more frequent double-layered sheets. (c) A similar aspect is obtained when calculating the sum of the map shown in (a) with its mirrored projection, thus simulating a double-layered sheet. The frame size of (a), (b) and (c) is that of one unit cell, 6.4 nm.

that MIP tetramers were precisely superimposed on each other. Calculating the averages corresponding to the two sets of correlation peaks yielded the two insets of Figure 7(a). Using these averaged topographs, the double-layered sheet was reconstructed. This model demonstrated that MIP tetramers from the apposing layers interact with each other in a "tongue-and-groove" fashion: the large protrusions in one membrane fit the small protrusions in the apposing membrane, and *vice versa* (Figure 7(b); white arrowhead).

Reconstituted sheets were further investigated by cryo-electron microscopy for two reasons: first, to verify that they were also double-layered in solution and that this was not an artefact of specimen preparation for AFM, and second to verify the exact superposition of MIP tetramers by analyzing their projection structure at high resolution. Edge-on views of sheets which were suspended in a thin layer of vitrified negative stain solution (Adrian *et al.*, 1998) confirmed that they indeed existed mostly as double-layered structures in solution (white arrowheads in Figure 8). Projection maps were calculated from sheets that were adsorbed to the carbon film and vitrified by rapid freezing. They fell into two categories: one exhibited eight density peaks arranged asymmetrically in the monomer (Figure 9(a)), whereas the other had eight densities arranged symmetrically about a mirror plane at 45° to the lattice (Figure 9(b)). The former was observed only rarely: its distinct handedness was similar to that of AQP1 (Walz *et al.*, 1995), and was likely to be derived from sheets with only one crystalline layer. In contrast, symmetrical projection maps were obtained more frequently and were consistent with the more abundant double-layered sheets, with tetramers of the two layers packed in register corresponding to space group $P422$. This assignment was supported by superpositioning the 0.57 nm asymmetric map with its own mirror image to simulate a double-layered sheet. The resulting projection map (Figure 9(c)) was indeed similar to the 0.69 nm symmetrical map in Figure 9(b) and to the 0.90 nm map presented previously (Hasler *et al.*, 1998). Therefore, the data obtained by cryo-electron microscopy strongly support the precise stacking of two MIP tetramers by the tongue-and-groove interaction of extracellular surfaces.

Discussion

Evidence obtained by atomic force and cryo-electron microscopy demonstrates that reconstituted square arrays of MIP can interact in a highly specific manner *via* their extracellular surfaces to form double-layered sheets. This supports the alleged ability of MIP to form membrane junctions (Bok *et al.*, 1982; Sas *et al.*, 1985). Our images show that the interaction between MIP tetramers is highly specific, insofar as they superimpose exactly, and bind to each other with their extra-

cellular surfaces in a tongue-and-groove fashion. This level of specificity is significant, and is more likely to represent an intrinsic property of MIP than merely an arbitrary aggregation of reconstituted membranes in the test tube.

Therefore MIP may function in the lens as a channel for water and selected small solutes, as well as serving for cell-cell adhesion which supports the tight packing of fiber cell layers (Bond *et al.*, 1996). Are these dual functions compatible with each other? For example, if all MIP molecules were involved in junction formation, how could MIP function as a channel allowing the diffusion of water and possibly certain solute molecules between the extracellular space and the cell cytoplasm? Immunolabeling experiments have shown that MIP is not restricted to membrane junctional domains but is present throughout the non-junctional membranes (Fitzgerald *et al.*, 1983; Paul & Goodenough, 1983; Varadaraj *et al.*, 1999). Hence, a sizable portion of MIP is available to serve as channels. An interesting novel option arises: if the precise superposition of MIP molecules as seen in reconstituted sheets occurred between adjacent fiber cells in the lens, it is conceivable that they could form continuous channels connecting the cell cytoplasms. This would provide an alternative path for water and possibly small solutes that also flow through the cell-cell gap junction channels, known to be composed of connexins.

The second important implication of the double-layered nature of MIP sheets is a technical one and concerns the interpretation of projection maps of MIP especially when it is compared with maps of other aquaporins. It was noted earlier (Hasler *et al.*, 1998) that the 0.90 nm projection of MIP exhibited a mirror plane at 45° to the lattice which was considerably stronger than that recognized in the projection map of AQP1. While at first glance this could reflect sequence and conformational differences between the isoforms, our results now show that this observed symmetry in the MIP monomer can be attributed to the double-layered nature of the reconstituted sheets. The projection map of MIP incorporates two tetramers facing each other with their extracellular surfaces, corresponding to space group $P422$. The stacking of MIP tetramers by a tongue-and-groove fit of their extracellular surfaces may also be a reason for the unidirectional packing of tetramers in single layers, which is different from that of the tetragonal 2D crystals of AQP1 and AQPZ (Ringler *et al.*, 1999) that pack with a $p42_12$ symmetry.

In conclusion, the crystallographic packing of two arrays of MIP implies a highly specific interaction between their extracellular surfaces. This lends further support to a dual function of MIP, as a water channel, and as a cell-cell adhesion molecule. The future 3D reconstruction from tilted views of these sheets has the potential to provide full structural details for both of these functions.

Materials and Methods

Purification and reconstitution of sheets with crystalline MIP

MIP was purified and crystallized as described by Hasler *et al.* (1998). In brief, lens membranes of the core were solubilized with octyl- β ,D-glucoside (OG) and directly loaded on a sucrose gradient with decyl- β ,D-maltoside as detergent. After overnight centrifugation the fractions enriched in MIP were further purified by cation-exchange chromatography. Pure MIP (>95%) was reconstituted with *E. coli* lipids solubilized in OG at a lipid-to-protein ratio of 1:1 (w/w). After a one hour incubation at room temperature, the samples were dialyzed against detergent-free crystallization buffer (10 mM Mes-NaOH (pH 6), 100 mM NaCl, 50 mM MgCl₂, 0.005% (w/v) NaN₃) at different temperatures for three days, and finally assayed by negative stain electron microscopy for the presence of sheets with crystalline arrays.

Atomic force microscopy and image processing

The stock solution of crystalline sheets (0.5–1 mg/ml protein) was diluted 20-fold in buffer A (10 mM Tris-HCl (pH 8.8), 150 mM KCl, 50 mM MgCl₂) or buffer B (20 mM Na-acetate-HCl (pH 5), 50 mM NaCl), depending on the experiment. A 20 μ l drop of this solution was deposited on freshly cleaved muscovite mica (Mica New York Corp., New York) prepared as previously described (Schabert & Engel, 1994). After 30 to 45 minutes, the sample was gently washed with the appropriate buffer to remove membranes that were not firmly attached to the substrate. Images were acquired with a commercial AFM (Nanoscope III, Digital Instruments, Santa Barbara, CA 93117, USA) equipped with a 120 μ m scanner (j-scanner) and a liquid cell. The liquid cell was operated without an O-ring seal. Oxide-sharpened Si₃N₄ cantilevers from Digital Instruments with a length of 120 μ m and a nominal spring constant of $k = 0.38$ N/m or from Olympus (Tokyo, Japan) with a length of 100 μ m and a force constant of $k = 0.1$ N/m were used. After a period of 15 to 30 minutes of thermal relaxation, initial engagement of the tip was achieved at scan size zero to minimize specimen deformation and tip contamination. Operation and calibration of the AFM was performed as described (Müller & Engel, 1997). High-resolution AFM images were recorded in the contact mode at forces between 50 and 150 pN applied to the tip. The optimal buffer conditions for high-resolution imaging were adjusted according to Müller *et al.*, 1999. Correlation averaging (Saxton & Baumeister, 1982) and single-particle analysis (Frank *et al.*, 1978; Schabert & Engel, 1994) were carried out with the SEMPER image processing system (Saxton *et al.*, 1979; Synoptics Ltd., Cambridge, UK). Images (512 \times 512 pixels) were flattened line by line prior to correlation averaging and single particle analysis. The lateral resolution of the calculated averages was either estimated from the powerspectrum of the raw images if the areas were coherent, or according to the FRC (Saxton & Baumeister, 1982), the PHR (Frank *et al.*, 1981), and the SSNR (Unser *et al.*, 1987), if the crystals were disordered. Simultaneously acquired trace and retrace images were processed separately. The calculated correlation averages were subsequently added together to compensate for friction effects (Schabert & Engel, 1994).

Perspective views of raw data were prepared using the AFM software supplied by Digital Instruments, while the model of a crystalline MIP double layer was

calculated using DINO, developed by Ansgar Philippsen (<http://www.bioz.unibas.ch/~xray/dino>).

In vitro and on mica digestion of MIP sheets by carboxypeptidase Y

Membranes after urea/alkali-stripping and 2D MIP crystals (Hasler *et al.*, 1998) were transferred into 12.5 mM Na-acetate-HCl, 5 mM Mes-NaOH (pH 6), 12.5 mM MgCl₂, 50 mM NaCl, 0.25 mM DTT. An aliquot of each sample was incubated overnight with 250 units of carboxypeptidase Y (Sigma, St. Louis, USA) at room temperature, the rest was incubated without carboxypeptidase Y overnight and was used as negative control. Stripped membranes were washed twice to remove the remaining carboxypeptidase Y while 2D crystals were not washed. Digested membranes were subsequently analyzed by SDS gel electrophoresis. Reconstituted membranes were further analyzed by Western blot with an antibody directed against the sequence VTGEPVEL located at the carboxyl tail of MIP (a kind gift of Dr Larry Takemoto, Kansas State University, Division of Biology, Manhattan, USA).

Reconstituted MIP sheets were adsorbed to mica and then incubated overnight at room temperature with at least 250 units of carboxypeptidase Y in 12.5 mM Na-acetate-HCl, 5 mM MES-NaOH (pH 6), 12.5 mM MgCl₂, 50 mM NaCl, 0.25 mM DTT, or in 25 mM Na-acetate-HCl (pH 6), 0.5 mM DTT (Walz *et al.*, 1996). After digestion, the sample was gently washed with buffer A and subsequently imaged in the same buffer.

Cryo-electron microscopy and image processing

For cryo-electron microscopy, MIP 2D crystals were adsorbed to pentylamine glow-discharged, carbon-coated grids (400 mesh), blotted with a filter paper for eight to ten seconds, and immediately frozen in liquid ethane (Dubochet *et al.*, 1988). Grids were mounted into a pre-cooled Gatan 626-DH Cryo-Holder (Gatan Inc., Pleasanton, CA) and transferred into a Hitachi H-8000 transmission electron microscope. Images were recorded on Kodak SO 163 sheet film at 200 kV acceleration voltage, at a nominal magnification of 50,000 \times , at a temperature of -182°C , and under low-dose conditions (500 electrons/nm²).

Micrographs were inspected by optical diffraction, and well-ordered areas were digitized with a Leafscan-45 (Leafscan Inc., Westborough, MA) scanner with a 0.2 nm pixel size at the sample level. Projections of ice-embedded samples were reconstructed using the MRC program suite for image processing (Crowther *et al.*, 1996). The projection map of MIP in single-layered sheets was calculated from a merged data set from seven micrographs where the phase residual in the resolution band between 0.57 and 0.62 nm exhibited a value of 78.8° (90° random) and the overall phase residual a value of 46.8° . Therefore, the projection map was calculated from the merged amplitudes and phases to a resolution of 0.57 nm, enforcing the p4 symmetry and compensating for the resolution-dependent fading of the diffraction amplitudes. For the projection map of double-layered MIP sheets, a merged data set from five images was taken. The phase residual in the resolution band between 0.69 and 0.80 nm exhibited a value of 67.8° and the overall phase residual a value of 42.9° . Hence, the projection map was calculated from the merged ampli-

tudes and phases to a resolution of 0.69 nm and 4-fold symmetrized.

Cryo-negative stain electron microscopy

For cryo-negative stain electron microscopy, the sample was exposed to staining solution (16% ammonium molybdate (pH 7)) in the holes of a perforated carbon film for 30 seconds and was quick-frozen in liquid ethane (Adrian *et al.*, 1998). These cryo-negative stain grids were mounted into a precooled Gatan 626-DH Cryo-Holder (Gatan Inc., Pleasanton, CA) operated at -182°C . Images were recorded on Kodak SO 163 sheet film with a Hitachi H-8000 transmission electron microscope operated at 100 kV and at 5000 \times nominal magnification under low-dose conditions (10 electrons/ nm^2).

Immunogold labeling and unidirectional shadowing

Reconstituted MIP sheets (0.5-1 mg/ml protein) were first diluted five times in crystallization buffer prior to adsorption on freshly cleaved mica for ten minutes. The sample was washed three times with 10 mM Hepes-NaOH (pH 7.2), 50 mM NaCl and then incubated with the primary antibody (1.74 mg/ml stock solution; diluted 1:10) for 30 minutes. After another washing step, the sample was incubated with the 15 nm goat-anti rabbit-immunogold secondary antibody for one hour. Mica plates were extensively washed, dried in air, and unidirectionally shadowed with Pt/C at an elevation of 20° in a BAF-300 (Balzers AG, Switzerland). Finally, the sample was coated with carbon, and the replica floated on a water surface and picked up by a copper grid. Micrographs were recorded at 40,000 \times or 50,000 \times magnification in a Hitachi H-7000 electron microscope operated at 100 kV using a dose of 2000 to 3000 electrons/ nm^2 .

The primary antibody, HNPA1, was directed against the sequence SGAHVNPVAVT located on the B-loop of the MIP molecule (a kind gift from Dr Ana B. Chepelinsky, National Eye Institute, NIH, Bethesda, USA).

Acknowledgments

This work was supported by the Swiss National Foundation for Scientific Research (grant 4036-44062 to A. E.) and the Health Research Council of New Zealand (J. K.). The authors gratefully acknowledge Drs Ana B. Chepelinsky at the National Eye Institute, NIH, Bethesda, USA and Larry Takemoto, Kansas State University, Division of Biology, Manhattan, USA for providing the antibodies used in this work. We thank Ansgar Philippsen for helping with DINO, Dr S. A. Müller for critical reading of the manuscript, and S. Scheuring for fruitful discussions.

References

- Adrian, M., Dubochet, J., Fuller, S. D. & Harris, J. R. (1998). Cryo-negative staining. *Micron*, **29**, 145-160.
- Bok, D., Dockstader, J. & Horwitz, J. (1982). Immunocytochemical localization of the lens main intrinsic polypeptide (MIP26) in communicating junctions. *J. Cell Biol.* **92**, 213-220.
- Bond, J., Green, C., Donaldson, P. & Kistler, J. (1996). Liquefaction of cortical tissue in diabetic and galactosemic rat lenses defined by confocal laser scanning microscopy. *Invest. Ophthalmol. Vis. Sci.* **37**, 1557-1565.
- Broekhuysse, R. M., Kuhlmann, E. D. & Stols, A. L. (1976). Lens membranes II. Isolation and characterization of the main intrinsic polypeptide (MIP) of bovine lens fiber membranes. *Expt. Eye Res.* **23**, 365-71.
- Chandy, G., Zampighi, G. A., Kreman, M. & Hall, J. E. (1997). Comparison of the water transporting properties of MIP and AQP1. *J. Membr. Biol.* **159**, 29-39.
- Costello, M. J., McIntosh, T. J. & Robertson, J. D. (1989). Distribution of gap junctions and square array junctions in the mammalian lens. *Invest. Ophthalmol. Vis. Sci.* **30**, 975-989.
- Crowther, R. A., Henderson, R. & Smith, J. M. (1996). MRC image-processing programs. *J. Struct. Biol.* **116**, 9-16.
- Dubochet, J., Adrian, M., Chang, J.-J., Homo, J.-C., Lepault, J., McDowell, A. W. & Schultz, P. (1988). Cryo-electron microscopy of vitrified specimens. *Quart. Rev. Biophys.* **21**, 129-228.
- Dunia, I., Manenti, S., Rousselet, A. & Benedetti, E. L. (1987). Electron microscopic observations of reconstituted proteoliposomes with the purified major intrinsic membrane protein of eye lens fibers. *J. Cell Biol.* **105**, 1679-1689.
- Ehring, G. R., Zampighi, G., Horwitz, J., Bok, D. & Hall, J. E. (1990). Properties of channels reconstituted from the major intrinsic protein of lens fiber membranes. *J. Gen. Physiol.* **96**, 631-664.
- Ehring, G. R., Lagos, N., Zampighi, G. & Hall, J. E. (1992). Phosphorylation modulates the voltage dependence of channels reconstituted from the major intrinsic protein of lens fiber membranes. *J. Membr. Biol.* **126**, 75-88.
- Fitzgerald, P. G., Bok, D. & Horwitz, J. (1983). Immunocytochemical localization of the main intrinsic polypeptide (MIP) in ultrathin frozen sections of rat lens. *J. Cell Biol.* **97**, 1491-1499.
- Frank, J., Goldfarb, W., Eisenberg, D. & Baker, T. S. (1978). Reconstruction of glutamine synthetase using computer averaging. *Ultramicroscopy*, **3**, 283-290.
- Frank, J., Verschoor, A. & Boublik, M. (1981). Computer averaging of electron micrographs of 40S ribosomal subunits. *Science*, **214**, 1353-1355.
- Gooden, M., Rintoul, D., Takehana, M. & Takemoto, L. (1985). Major intrinsic polypeptide (MIP26K) from the lens membrane: reconstitution into vesicles and inhibition of channel forming activity by peptide antiserum. *Biochem. Biophys. Res. Com.* **128**, 993-999.
- Gorin, M. B., Yancey, S. B., Cline, J., Revel, J.-P. & Horwitz, J. (1984). The major intrinsic protein (MIP) of the bovine lens fiber membrane: characterization and structure based on cDNA cloning. *Cell*, **39**, 49-59.
- Grujters, W. T. M., Kistler, J., Bullivant, S. & Goodenough, D. A. (1987). Immunolocalization of MP70 in lens fiber 16-17 nm intercellular junctions. *J. Cell Biol.* **104**, 565-572.
- Hasler, L., Walz, T., Tittmann, P., Gross, H., Kistler, J. & Engel, A. (1998). Purified lens major intrinsic protein (MIP) forms highly ordered tetragonal two-dimensional arrays by reconstitution. *J. Mol. Biol.* **279**, 855-864.
- Hoh, J. H., Lal, R., John, S. A., Revel, J. P. & Arnsdorf, M. F. (1991). Atomic force microscopy and dissection of gap junctions. *Science*, **253**, 1405-1408.

- Keeling, P., Johnson, K., Sas, D., Klukas, K., Donahue, P. & Johnson, R. (1983). Arrangement of MP26 in lens junctional membranes: analysis with proteases and antibodies. *J. Membr. Biol.* **74**, 217-228.
- Kistler, J., Kirkland, B. & Bullivant, S. (1985). Identification of a 70,000-D protein in lens membrane junctional domains. *J. Cell Biol.* **101**, 28-35.
- Kushmerick, C., Rice, S. J., Baldo, G. J., Haspel, H. C. & Mathias, R. T. (1995). Ion, water and neutral solute transport in *Xenopus* oocytes expressing frog lens MIP. *Expt. Eye Res.* **61**, 351-362.
- Lee, M. D., King, L. S. & Agre, P. (1997). The aquaporin family of water channel proteins in clinical medicine. *Medicine*, **76**, 141-156.
- Mathias, R. T., Rae, J. L. & Baldo, G. J. (1997). Physiological properties of the normal lens. *Physiol. Rev.* **77**, 21-50.
- Modesto, E., Lampe, P. D., Ribeiro, M. C., Spray, D. C. & Campos de Carvalho, A. C. (1996). Properties of chicken lens MIP channels reconstituted into planar lipid bilayers. *J. Membr. Biol.* **154**, 239-249.
- Mulders, S. M., Preston, G. M., Deen, P. M. T., Guggino, W. B., van Os, C. H. & Agre, P. (1995). Water channel properties of major intrinsic protein of lens. *J. Biol. Chem.* **270**, 9010-9016.
- Müller, D. J. & Engel, A. (1997). The height of biomolecules measured with the atomic force microscope depends on electrostatic interactions. *Biophys. J.* **73**, 1633-1644.
- Müller, D. J., Fotiadis, D., Scheuring, S., Müller, S. A. & Engel, A. (1999). Electrostatically balanced subnanometer imaging of biological specimens by atomic force microscope. *Biophys. J.* **76**, 1101-1111.
- Park, J. H. & Saier, M. H. (1996). Phylogenetic characterization of the MIP family of transmembrane channel proteins. *J. Membr. Biol.* **153**, 171-180.
- Paul, D. L. & Goodenough, D. A. (1983). Preparation, characterization, and localization of antisera against bovine MIP26, an integral protein from lens fiber plasma membrane. *J. Cell. Biol.* **96**, 625-632.
- Ringler, P., Borgnia, M. J., Stahlberg, H., Maloney, P. C., Agre, P. & Engel, A. (1999). Structure of the water channel AqpZ from *Escherichia coli* revealed by electron crystallography. *J. Mol. Biol.* **291**, 1181-1190.
- Sas, D. F., Sas, J., Johnson, K. R., Menko, A. S. & Johnson, R. G. (1985). Junctions between lens fiber cells are labeled with a monoclonal antibody shown to be specific for MP26. *J. Cell. Biol.* **100**, 216-225.
- Saxton, W. O. & Baumeister, W. (1982). The correlation averaging of a regularly arranged bacterial cell envelope protein. *J. Microsc.* **127**, 127-138.
- Saxton, W. O., Pitt, T. J. & Horner, M. (1979). Digital image processing: the SEMPER system. *Ultramicroscopy*, **4**, 343-354.
- Scaglione, B. A. & Rintoul, D. A. (1989). A fluorescence-quenching assay for measuring permeability of reconstituted lens MIP26. *Invest. Ophthalmol. Vis. Sci.* **30**, 961-966.
- Schabert, F. A. & Engel, A. (1994). Reproducible acquisition of *Escherichia coli* porin surface topographs by atomic force microscopy. *Biophys. J.* **67**, 2394-2403.
- Schabert, F. A., Henn, C. & Engel, A. (1995). Native *Escherichia coli* OmpF porin surfaces probed by atomic force microscopy. *Science*, **268**, 92-94.
- Shen, L., Shrager, P., Girsch, S. J., Donaldson, P. J. & Peracchia, C. (1991). Channel reconstitution in liposomes and planar lipid bilayers with HPLC-purified MIP26 of bovine lens. *J. Membr. Biol.* **124**, 21-32.
- Shiels, A. & Bassnett, S. (1996). Mutations in the founder of the MIP gene family underlie cataract development in the mouse. *Nature Genet.* **12**, 212-215.
- Unser, M., Trus, B. L. & Steven, A. C. (1987). A new resolution criterion based on spectral signal-to-noise ratios. *Ultramicroscopy*, **23**, 39-52.
- Varadaraj, K., Kushmerick, C., Baldo, G. J., Bassnett, S., Shiels, A. & Mathias, R. T. (1999). The role of MIP in lens fiber cell membrane transport. *J. Membr. Biol.* **170**, 191-203.
- Walz, T., Typke, D., Smith, B. L., Agre, P. & Engel, A. (1995). Projection map of aquaporin-1 determined by electron crystallography. *Nature Struct. Biol.* **2**, 730-732.
- Walz, T., Tittmann, P., Fuchs, K. H., Müller, D. J., Smith, B. L., Agre, P., Gross, H. & Engel, A. (1996). Surface topographies at subnanometer-resolution reveal asymmetry and sidedness of aquaporin-1. *J. Mol. Biol.* **264**, 907-18.
- Zampighi, G. A., Simon, S. A., Robertson, J. D., McIntosh, T. J. & Costello, M. J. (1982). On the structural organization of isolated bovine lens fiber junctions. *J. Cell Biol.* **93**, 175-189.
- Zampighi, G. A., Hall, J. E., Ehring, G. R. & Simon, S. A. (1989). The structural organization and protein composition of lens fiber junctions. *J. Cell. Biol.* **108**, 2255-75.
- Zampighi, G. A., Simon, S. A. & Hall, J. E. (1992). The specialized junctions of the lens. *Int. Rev. Cytol.* **136**, 185-225.

Edited by G. V. Heijne

(Received 20 March 2000; received in revised form 2 June 2000; accepted 2 June 2000)